

Correlated Octahedral Rotation and Organic Cation Reorientation Assist Halide Ion Migration in Lead Halide Perovskites

Manas Likhit Holekevi Chandrappa, Zhuoying Zhu, David P. Fenning, and Shyue Ping Ong*



Cite This: <https://doi.org/10.1021/acs.chemmater.1c01175>



Read Online

ACCESS |



Metrics & More

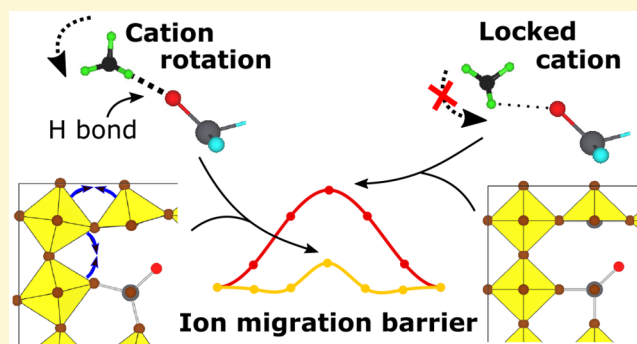


Article Recommendations



Supporting Information

ABSTRACT: Increasing the stability of lead halide perovskites (LHPs) is critical for their practical application in solar cells and other technologies. Halide ion migration is one of the main contributors to instability and hysteresis in LHP solar cells. Here, we employ a series of *Gedankenexperiments* to quantitatively establish the correlated effects of the A site cation motion, H bonding strength, and octahedral rotation on halide ion migration in APbBr_3 ($A = \text{Cs}$ or methylammonium/MA) LHPs. We find that in cubic CsPbBr_3 , the increase of PbBr_6 octahedra rotation/tilting during ion migration lowers the halide ion migration barrier by at least 100 meV compared to the orthorhombic phase. In MAPbBr_3 , we show that halide ion migration is also assisted by MA cation rotation to re-establish H bonding, resulting in lower halide migration barriers. These results suggest that “locking” the organic cation via chemical and processing means can help mitigate halide migration-induced instability and reduced hysteresis in LHP solar cells.



INTRODUCTION

Lead halide APbX_3 perovskite (LHP) solar cells have rapidly risen in the ranks of photovoltaic (PV) technologies over the past decade. The certified power conversion efficiency (PCE) of LHPs has exceeded 25%¹ and is now on par with the record performances of silicon solar cells. The hybrid organic–inorganic perovskites (HOIPs), which contain an organic cation such as methylammonium (CH_3NH_3^+ or MA) or formamidinium ($\text{NH}_2\text{CHNH}_2^+$ or FA) on the A site, have higher PCEs compared to inorganic LHP solar cells. However, their instability in the presence of moisture or air or even under illumination^{2–5} has become a major roadblock toward their commercialization. Therefore, increasing efforts are being devoted toward the development of inorganic LHPs, and their PCEs have been steadily on the rise.^{6–8}

LHP solar cells suffer from hysteresis. A major contributor is the migration of the halide ion,⁹ which is also responsible for phase segregation in mixed halide perovskites^{10,11} and degradation of HOIP light emitting diodes (PeLEDs) under electric bias.¹² Previous density functional theory (DFT) calculations have found low vacancy formation energies^{13,14} coupled with low migration barriers for halide ions in LHPs.^{15–17} Reducing ion migration has been shown to enhance the stability of LHPs.¹⁸ In particular, octahedral tilting/rotation and H bonding have been shown to stabilize the LHP structure.^{19–21} However, their role during the halide ion migration has not been systematically investigated. Lai et al.²² used classical force fields to simulate anion interdiffusion at the CsPbI_3 – CsPbBr_3 heterojunction and observed weak

coupling between low-frequency octahedral tilting modes and the surrounding lattice during vacancy hopping. Oranskaia et al. have also compared halide ion migration in MAPbBr_3 and FAPbBr_3 and attributed the lower halide migration barrier in MAPbBr_3 to a lower H bonding energy.²³ Nevertheless, much remains unknown about the potential coupling between octahedral tilting/rotation and H bonding and its consequent effect on halide migration barriers in organic as well as inorganic LHPs.

In this work, we use a series of *Gedankenexperiments* to quantitatively establish the correlated effects of the A site cation motion, H bonding strength, and octahedral rotation on halide ion migration in LHPs. As CsPbBr_3 and MAPbBr_3 exhibit higher stability and higher resistance to degradation under ambient conditions when compared to the iodide counterparts,^{24–28} we have selected these LHPs as the model systems for our study. We show that in inorganic CsPbBr_3 , cooperative correlated octahedral rotation in the cubic phase lowers the halide migration barrier when compared to the orthorhombic phase. In HOIP, we find that the extent of disruption of H bonding during ion migration is another major

Received: April 4, 2021

Revised: May 29, 2021



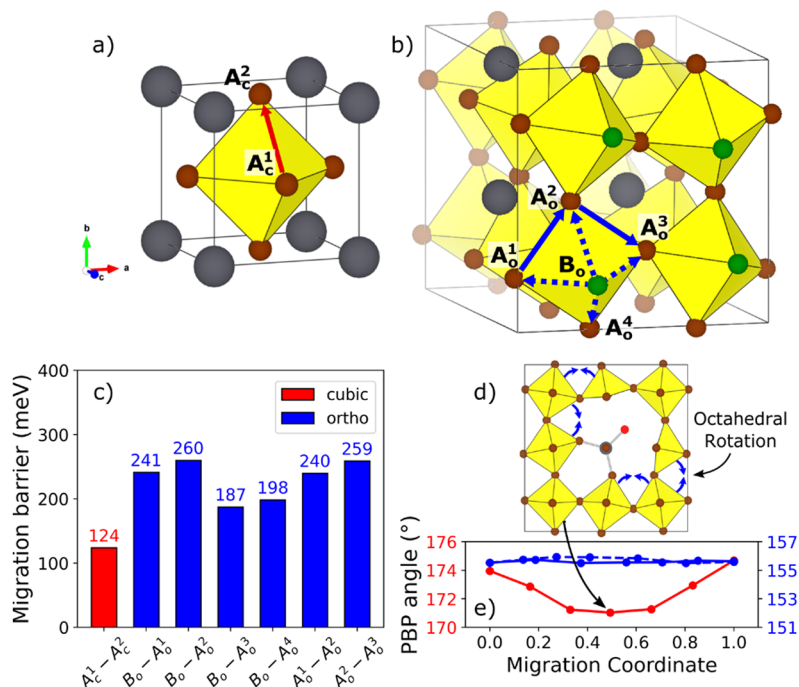


Figure 1. Br⁻ vacancy migration paths in the (a) cubic and (b) orthorhombic CsPbBr₃. In the cubic phase, there is only one symmetrically distinct path A_c¹-A_c². In the orthorhombic phase, there are six distinct pathways, four between nonequivalent sites B_o and A_o (dashed arrows) and two between equivalent A_o sites (solid arrows). (c) Comparison of kinetically resolved migration barriers in cubic and orthorhombic phases. (d) 2D projection of the transition state structure in cubic CsPbBr₃. (e) The average Pb-Br-Pb bond angle as a function of migration coordinate in the cubic (solid red) and orthorhombic phase for path B_o-A_o¹ (dashed blue) and A_o¹-A_o² (solid blue).

factor in determining the halide migration barrier. Based on these results, we speculate that low-symmetry perovskites would have higher halide ion migration barriers and hence can be used to design low-hysteresis PSCs.

METHODS

The DFT calculations were performed using the Vienna *Ab initio* Simulation Package (VASP)²⁹ within the projector augmented wave³⁰ approach. The exchange-correlation was modeled using the Perdew-Burke-Ernzerhof (PBE) Generalized Gradient Approximation (GGA)³¹ functional.

Climbing image nudged elastic band³² (CI-NEB) calculations of halide vacancy migration barriers were performed on a 3 × 3 × 3 supercell (27 formula units) for cubic perovskites (CsPbBr₃ and MAPbBr₃) and 2 × 2 × 1 supercell (16 formula units) for orthorhombic CsPbBr₃. Γ -centered *k*-point meshes of 1 × 1 × 1 and 1 × 1 × 2 were used for cubic and orthorhombic supercells, respectively. The energy cutoff was set at 520 eV, and the force convergence criterion was 0.02 eV atom⁻¹. All analysis was performed using the Python Materials Genomics (pymatgen) library.³³

The strength of hydrogen bonding between MA cations and the inorganic framework was determined using the scheme developed by Svane et al.³⁴ In this method, the monopole term of the electrostatic interaction between the organic cation and anionic framework is removed such that only the dipolar and higher order terms of hydrogen bonding are obtained. This method was used to quantify the change in the H bonding energy in MAPbBr₃ during ion migration in this work. The complete details of these calculations are presented in the Supporting Information.

RESULTS

Br⁻ Vacancy Migration Barriers in CsPbBr₃. Figures 1a and 1b show the distinct migration pathways for the Br⁻ vacancy migration in cubic and orthorhombic CsPbBr₃, respectively. In cubic CsPbBr₃, all Br sites are symmetrically

equivalent with only one distinct path, A_c¹-A_c². In orthorhombic CsPbBr₃, there are two symmetrically distinct Br sites (A_o and B_o) and six distinct migration paths. Given that symmetrically distinct sites have different energies, the kinetically resolved activation barrier,³⁵ which is the average of the migration barriers of the forward and backward hops (see Figure S2), is reported here.

Figure 1c compares the Br⁻ vacancy migration barriers in cubic and the orthorhombic CsPbBr₃. The calculated migration barrier in cubic CsPbBr₃ is 124 meV, while the calculated migration barriers in orthorhombic CsPbBr₃ are much higher, ranging between 187 and 260 meV. To probe the factors contributing to the large difference in the migration barrier in the two phases, the average of all the Pb-Br-Pb bond angles was used as a metric to quantify the amount of octahedral rotation/tilt present in a structure. The average Pb-Br-Pb bond angles in the defect-free cubic and orthorhombic structure are 180° and 156°, respectively. Figure 1e shows the average of the Pb-Br-Pb angles as a function of migration coordinate in cubic and orthorhombic CsPbBr₃ (paths B_o-A_o¹ and A_o¹-A_o²). For cubic CsPbBr₃, the average Pb-Br-Pb angle decreases by about 2°, reaching a minimum at the transition state (shown in Figure 1d), during Br⁻ migration but remains constant for the orthorhombic phase. We may therefore hypothesize that the well-known decrease in the energy of perovskites due to octahedral rotation^{20,36-39} during ion migration in the cubic phase results in a lower migration barrier than in the orthorhombic phase.

Figure 2 compares the CI-NEB barriers for Br⁻ vacancy migration barriers in cubic and orthorhombic phases where successive shells of PbBr₆ octahedra were allowed to relax (all Cs atoms were always allowed to relax). The octahedron to which the migrating ion belongs is denoted as the “0th shell”.

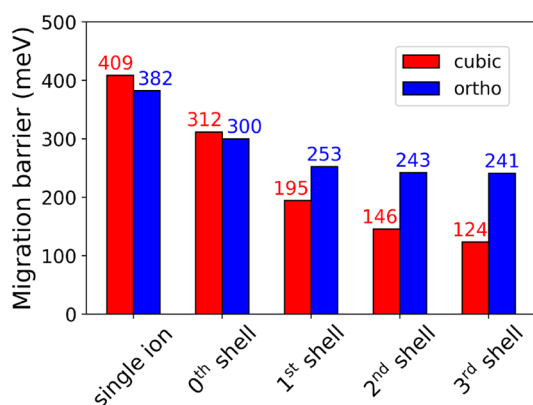


Figure 2. Shellwise relaxation NEB migration barriers in cubic and orthorhombic phase (path $B_0-A_0^{\ddagger}$).

The octahedra sharing corners with the 0th shell are denoted as the “1st shell”, and the ones sharing corners with the “1st shell” are denoted as “2nd shell octahedra”. It is clear that allowing successive shells around the migration path to relax has a significantly larger effect on the Br^- migration barrier in the cubic phase. For example, when all octahedra are frozen (denoted as “single ion relaxation”), the barrier for path $B_0-A_0^{\ddagger}$ in the orthorhombic phase (382 meV) is similar to those in the cubic phase (409 meV). Allowing the 0th shell to relax decreases the Br^- migration barrier in both phases by approximately 100 meV. However, allowing the 1st shell to relax decreases the migration barrier in the cubic phase by more than 100 meV while the migration barrier in the orthorhombic phases decreases by only 47 meV. Relaxing the 2nd and 3rd shells further decreases the migration barrier by 71 meV in the cubic phase, but it decreases only by 12 meV in

the orthorhombic phase. Similar results were obtained for other paths in the orthorhombic phase as shown in Figure S4.

Br^- Vacancy Migration Barriers in $MAPbBr_3$. In cubic $MAPbBr_3$, the perovskite “A” site is occupied by MA^+ instead of Cs^+ . At room temperature, the MA cations are free to rotate, resulting in orientational dynamic disorder. However, upon application of the electric field during cell operation, these MA cations will align in the direction of the electric field because of their dipole.⁴⁰ In this work, the ion migration barriers were obtained with all MA cations oriented along the $\langle 100 \rangle$ direction, in line with the previous work by Luo et al.⁴⁰ Figure 3a shows the crystal structure of cubic $MAPbBr_3$ and the distinct Br^- vacancy migration paths. Due to the symmetry breaking by the aligned MA cations, the three paths A–B–A, A–C–A, and C–B–C are all distinct. Paths A–B–A and A–C–A are parallel to the C–N bond of the MA while path C–B–C is perpendicular to the C–N bond. From Figure 3, we may observe that the three distinct migration paths have barriers ranging from 345 to 467 meV. It should be noted that all three paths are not symmetric about the midpoint of the migration coordinate due to the orientation of the MA cation.

Figures 4a, b, and c show the average Pb–Br–Pb angle as a function of migration coordinate for paths A–B–A, A–C–A, and C–B–C, respectively. The migration coordinates corresponding to transition states (saddle point with maxima in energy) are indicated by the shaded regions. It is evident that Br^- vacancy migration along path A–B–A is accompanied by a considerable increase in the octahedral rotation (1° decrease in the average Pb–Br–Pb angle) at the transition state. The other two paths show smaller increases in the octahedral rotation at the transition state ($\sim 0.5^\circ$ and 0.25° decrease in the average Pb–Br–Pb angle in paths A–C–A and C–B–C, respectively). Similar to $CsPbBr_3$, we speculate that

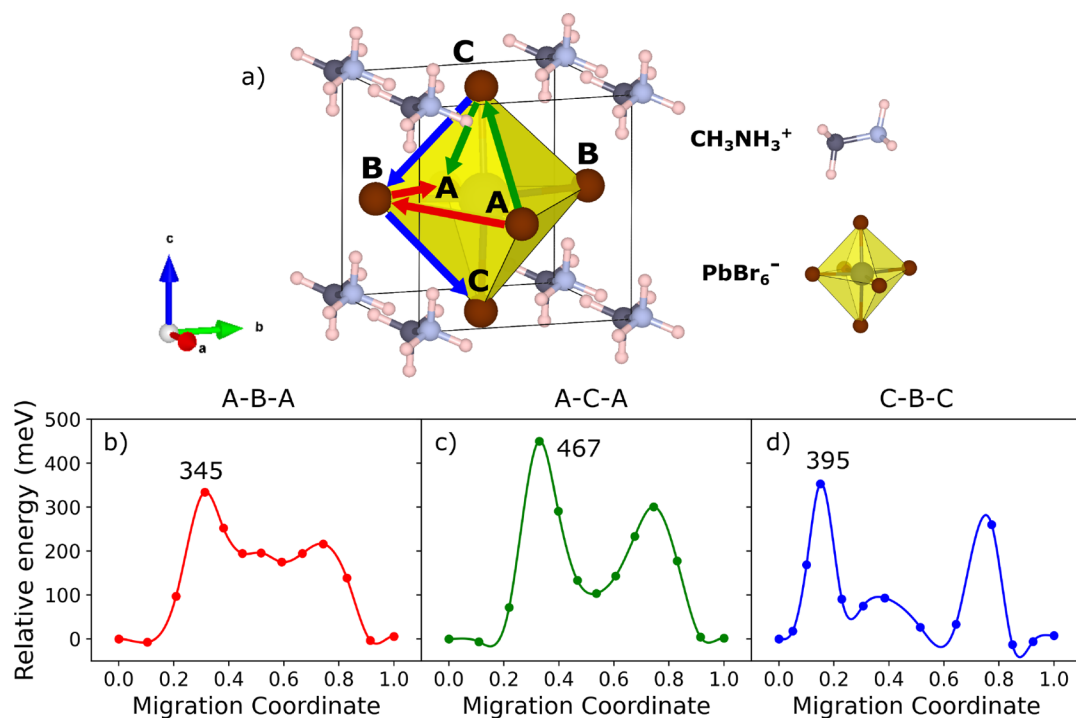


Figure 3. Br^- vacancy migration paths in cubic $MAPbBr_3$. Paths A–B–A (red) and A–C–A (green) are parallel to the C–N bond in the MA cation whereas path C–B–C (blue) is perpendicular to the C–N bond. Energy along the minimum energy path for paths (b) A–B–A, (c) A–C–A, and (d) C–B–C.

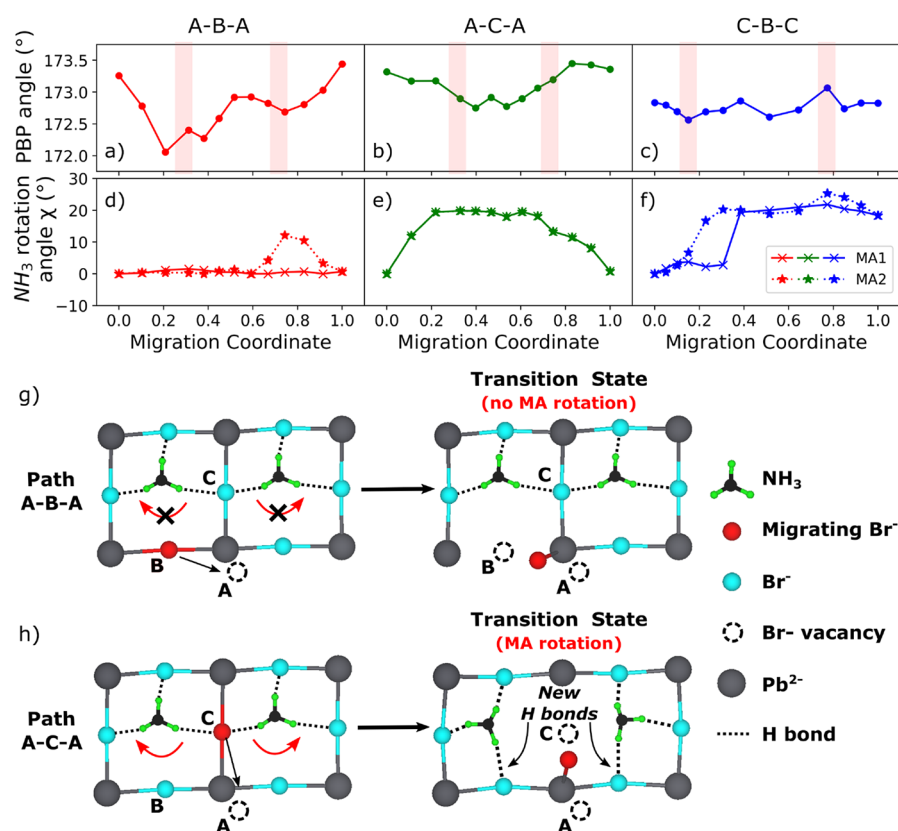


Figure 4. Average Pb–Br–Pb bond angle (top panel) and angle of rotation NH₃ group (χ) with crystallographic *a* direction as the axis of rotation (bottom panel) as a function of the migration coordinate for paths A–B–A, A–C–A, and C–B–C. Initial end point structure for paths (g) A–B–A and (h) A–C–A along with the transition state structure. In path A–C–A the ion migration is accompanied by MA rotation whereas there is no MA rotation in path A–B–A.

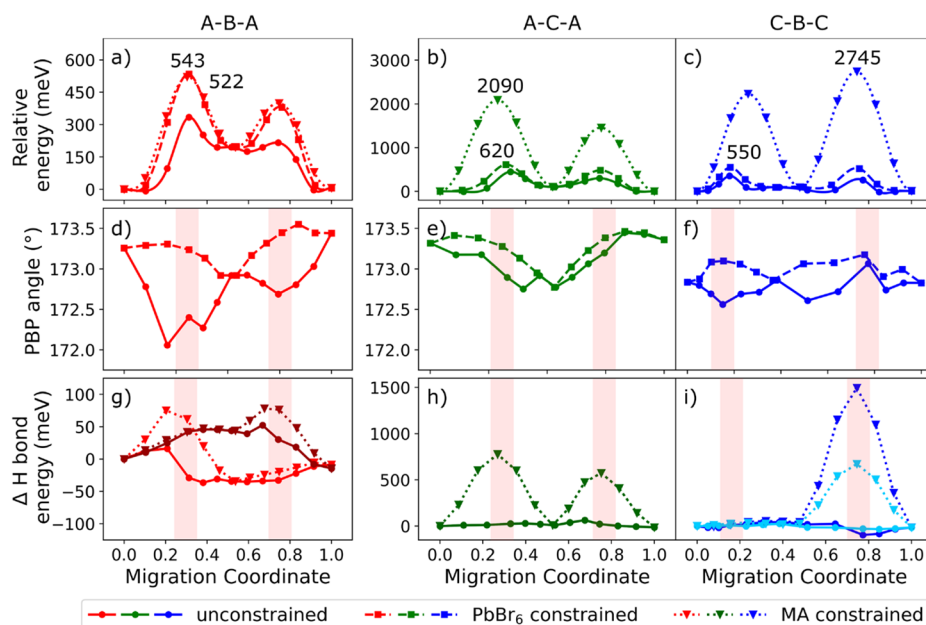


Figure 5. Energy along migration paths (a) A–B–A, (b) A–C–A, and (c) C–B–C from unconstrained, PbBr₆-constrained, and MA-constrained NEB calculations. Average Pb–Br–Pb bond angle as a function of migration coordinate for unconstrained and PbBr₆-constrained calculations for (d) A–B–A, (e) A–C–A, and (f) C–B–C. Comparison of the change in H bond energy of individual MA cations as a function of the migration coordinate between unconstrained and MA-constrained calculations for (g) A–B–A, (h) A–C–A, and (i) C–B–C. Different color shades in (g) and (i) represent data for two different MA cations.

octahedral rotation contributes to the slightly lower ion migration barrier for path A–B–A compared to paths A–C–A and C–B–C.

In addition to octahedral rotation, there are differences in the motion of two MA cations during ion migration. Figure S5a shows angles ϕ , θ , and χ used to specify the orientation of the MA cation in the structure. Angle θ is the angle made by projection of the C–N bond on the crystallographic a – b plane (see Figure 3) with respect to the a axis. Angle ϕ is the angle made by the C–N bond with respect to the c axis, and χ is the angle of rotation of the NH₃ group with respect to its initial position during ion migration with the a direction as the axis of rotation. Figures 4d–f show χ as a function of migration coordinate for the two MA cations (MA1 and MA2) that showed significant reorientation during ion migration in the three paths. Plots for the variation of ϕ and θ are given in Figure S5. It may be observed that paths A–C–A and C–B–C exhibit much larger MA reorientation compared to path A–B–A. This difference in MA reorientation can be understood in terms of the differences in the migration paths. From Figure 4g, it may be observed that in path A–B–A, the Br[−] moves entirely in a plane that is parallel to the aligned MA cations. Throughout the migration pathway, the Br[−] is sufficiently far away from the H atoms in the MA groups such that there is little/no change in H bonding. Hence, there are only small variations in ϕ along the migration path. In contrast, the path A–C–A involves Br[−] at site C that is initially H bonded to MA moving to site A. The motion of the Br[−] causes the rotation of the MA group with the concurrent breaking and formation of H bonds, as shown in Figure 4h. This results in much larger variations in ϕ , θ , and χ along the migration path. The same effect is present in path C–B–C (see Figure S6).

To decouple the effect of octahedral and MA rotations on the migration barrier, selective dynamics NEB calculations were performed in which the PbBr₆ octahedra or MA cations were frozen, denoted as “PbBr₆-constrained” and “MA-constrained” NEB calculations, respectively, in Figures 5a–c. The values of the migration barriers are tabulated in Table S1. When the PbBr₆ octahedra are constrained, path A–B–A has the highest increase in the migration barrier of 198 meV. When the MA movement is constrained, there is a huge increase of 1623 and 2350 meV for paths A–C–A and C–B–C, respectively, and a relatively small increase of only 177 meV for path A–B–A. These results are consistent with the fact that path A–B–A exhibits the largest changes in PBP bond angle, while paths A–C–A and C–B–C exhibit the largest changes in MA rotation. By constraining the rotation of PbBr₆ octahedra, the magnitude of the change in PBP angle along the A–B–A migration path becomes similar to that in paths A–C–A and C–B–C, resulting in a large increase in migration barrier (see Figures 5d–f). Constraining PbBr₆ octahedra rotation has a relatively smaller effect on the total H bonding energy (see Figures S7a–c).

Figures 5g–i show the change in H bonding energy as a function of migration coordinate for individual MA cations with significant change in H bonding energy at the transition state from unconstrained and MA-constrained NEB calculations. For path A–B–A, the H bonding energy decreases by only 30–50 meV at the transition state. In path A–C–A, there is a huge decrease in the H bonding energy of rotating MA cations (MA1 and MA2) of 600 meV. The positions of the two MAs is symmetric to the Br[−] vacancy migration path and hence have a similar ΔH energy profile. Similarly, in path C–

B–C, large changes in H bonding energies are observed when MA rotation is constrained compared to the unconstrained calculations. Constraining MA rotation only has a small effect on the changes in average Pb–Br–Pb angle as a function of migration coordinate (see Figures S7d–f).

DISCUSSION

By contrasting our NEB calculations in the inorganic CsPbBr₃ and the hybrid organic–inorganic MAPbBr₃ perovskites, we can derive new insights into the factors that influence Br[−] migration barriers in these materials. While PbBr₆ octahedral rotation is common to both types of perovskites, MAPbBr₃ also exhibits MA rotation and H bonding.

It is clear that octahedra rotation has a major cooperative role in both types of perovskites. When PbBr₆ octahedra (up to 2nd shell), especially those that are in the immediate vicinity of the migrating Br[−], are constrained against rotation, significant increases in migration barriers of ~100–200 meV are observed in cubic CsPbBr₃ and the paths in MAPbBr₃ where H bonding plays a smaller role (e.g., path A–B–A). In orthorhombic CsPbBr₃, a smaller degree of PbBr₆ octahedra rotation is observed with Br[−] migration; as a result, the migration barriers are higher but also exhibit smaller changes with constraining PbBr₆ motion. Hence, the ability of the cubic phase to accommodate low-frequency octahedral rotation modes facilitates anion migration, which is also noted in a previous study by Lai et al.²⁷

In MAPbBr₃, it is clear that another major factor influencing the Br[−] migration barrier is H bonding, which is the driving force behind MA rotation in certain paths. For paths where Br[−] migration is accompanied by MA rotation, constraining MA rotation results in a substantial change in H bonding (large δH bond) resulting in a more than 1000 meV increase in migration barriers. The total ΔH bond energy values are 203, 233, and 183 meV at the transition state for paths A–B–A, A–C–A, and C–B–C, respectively. Hence, we find that the path A–C–A, which has the highest ion migration barrier, also has the maximum disruption of H bonding during ion migration.

The results in this work suggest that efforts to limit halide migration in the organic–inorganic halide perovskites should be targeted at “locking” the organic cation. While the application of an electric field may be used to align the organic cations (e.g., MA), the result is field-assisted Br[−] migration in the preferred direction of organic cation alignment.⁴⁰ The locking of the organic cation may be achieved via chemical means, e.g., mixing of organic and inorganic cations,^{41–43} or processing means, e.g., application of pressure.^{44,45} Application of pressure on cubic MAPbBr₃ causes a phase transition to the orthorhombic phase and achieves the desired outcome of “locking” of the organic cations in specific orientations.⁴⁴ The enhanced interaction of the NH₃ group with halide ions by mean of H bonding has been identified as the cause of this ordering. Ghosh et al.⁴⁶ found that the substitution of the smaller Cs⁺ cation in low concentration (10%) in FAPbI₃ lowers the crystal symmetry and reduces the rocking motion of the octahedra. Additionally, sluggish cation dynamics has also been observed in FA/MA/Cs mixed perovskites⁴⁷ where experimental⁴⁸ and computational spectroscopies⁴⁶ show evidence of N–H bond stretching. This indicates an increase in the strength and number of H bonds between organic cations and halides in the inorganic framework, which can also achieve the locking of

theorganic cations in specific orientations.⁴⁶ Based on our study, these structural changes should increase ion migration barriers and perhaps explain the suppression of ion migration observed in mixed cation perovskites.

CONCLUSION

To conclude, we have performed a detailed study of Br⁻ migration in cubic and orthorhombic CsPbBr₃ and MAPbBr₃ using NEB calculations. In inorganic CsPbBr₃, cooperative correlated octahedral rotation in the cubic phase lowers the halide migration barrier when compared to the orthorhombic phase. In MAPbBr₃, the extent of disruption of H bonding during ion migration is the major factor in determining the halide migration barrier. The results suggest that developing low-symmetry LHPs with “locked” organic cations via composition tuning or processing is a potential pathway to reducing hysteresis in LHP-based solar cells.

ASSOCIATED CONTENT

Supporting Information

The Supporting Information is available free of charge at <https://pubs.acs.org/doi/10.1021/acs.chemmater.1c01175>.

H bonding strength calculation; kinetically resolved activation barrier calculation; octahedra shell division in cubic and orthorhombic CsPbBr₃; shellwise relaxed NEB barriers in orthorhombic CsPbBr₃; MA orientation angles; initial end point and transition state structure in path C–B–C in cubic MAPbBr₃; comparison of ΔH bonding energy and Pb–Br–Pb between unconstrained and constrained NEB calculations; MAPbBr₃-constrained NEB migration barriers (PDF)

AUTHOR INFORMATION

Corresponding Author

Shyue Ping Ong – Department of NanoEngineering, University of California San Diego, La Jolla, California 92093 0448, United States; orcid.org/0000-0001-5726-2587; Email: ongsp@eng.ucsd.edu

Authors

Manas Likhith Holekevi Chandrappa – Department of NanoEngineering, University of California San Diego, La Jolla, California 92093 0448, United States; orcid.org/0000-0002-7397-3087

Zhuoying Zhu – Department of NanoEngineering, University of California San Diego, La Jolla, California 92093 0448, United States; orcid.org/0000-0003-1775-7651

David P. Fenning – Department of NanoEngineering, University of California San Diego, La Jolla, California 92093 0448, United States; orcid.org/0000-0002-4609-9312

Complete contact information is available at: <https://pubs.acs.org/doi/10.1021/acs.chemmater.1c01175>

Notes

The authors declare no competing financial interest.

ACKNOWLEDGMENTS

This work was primarily supported by the Materials Project, funded by the U.S. Department of Energy, Office of Science, Office of Basic Energy Sciences, Materials Sciences and Engineering Division under contract no. DE-AC02-05-

CH11231: Materials Project program KC23MP. A portion of the computations performed in this work also used the Extreme Science and Engineering Discovery Environment (XSEDE), which is supported by National Science Foundation grant number ACI-1053575.

REFERENCES

- (1) Best Research-Cell Efficiency Chart. <https://www.nrel.gov/pv/cell-efficiency.html> (accessed 2021–03–28).
- (2) Aristidou, N.; Sanchez-Molina, I.; Chotchuangchutchaval, T.; Brown, M.; Martinez, L.; Rath, T.; Haque, S. A. The Role of Oxygen in the Degradation of Methylammonium Lead Trihalide Perovskite Photoactive Layers. *Angew. Chem., Int. Ed.* **2015**, *54*, 8208–8212.
- (3) Smecca, E.; Numata, Y.; Deretzis, I.; Pellegrino, G.; Boninelli, S.; Miyasaka, T.; La Magna, A.; Alberti, A. Stability of Solution-Processed MAPbI₃ and FAPbI₃ Layers. *Phys. Chem. Chem. Phys.* **2016**, *18*, 13413–13422.
- (4) Wang, D.; Wright, M.; Elumalai, N. K.; Uddin, A. Stability of Perovskite Solar Cells. *Sol. Energy Mater. Sol. Cells* **2016**, *147*, 255–275.
- (5) Kim, H.-S.; Seo, J.-Y.; Park, N.-G. Material and Device Stability in Perovskite Solar Cells. *ChemSusChem* **2016**, *9*, 2528–2540.
- (6) Wang, Y.; Zhang, T.; Kan, M.; Zhao, Y. Bifunctional Stabilization of All-Inorganic α -CsPbI₃ Perovskite for 17% Efficiency Photovoltaics. *J. Am. Chem. Soc.* **2018**, *140*, 12345–12348.
- (7) Li, X.; Tan, Y.; Lai, H.; Li, S.; Chen, Y.; Li, S.; Xu, P.; Yang, J. All-Inorganic CsPbBr₃ Perovskite Solar Cells with 10.45% Efficiency by Evaporation-Assisted Deposition and Setting Intermediate Energy Levels. *ACS Appl. Mater. Interfaces* **2019**, *11*, 29746–29752.
- (8) Yuan, H.; Zhao, Y.; Duan, J.; Wang, Y.; Yang, X.; Tang, Q. All-Inorganic CsPbBr₃ Perovskite Solar Cell with 10.26% Efficiency by Spectra Engineering. *J. Mater. Chem. A* **2018**, *6*, 24324–24329.
- (9) Li, C.; Tscheuschner, S.; Paulus, F.; Hopkinson, P. E.; Kiefling, J.; Köhler, A.; Vaynzof, Y.; Huettner, S. Iodine Migration and Its Effect on Hysteresis in Perovskite Solar Cells. *Adv. Mater.* **2016**, *28*, 2446–2454.
- (10) Zhang, H.; Fu, X.; Tang, Y.; Wang, H.; Zhang, C.; Yu, W. W.; Wang, X.; Zhang, Y.; Xiao, M. Phase Segregation Due to Ion Migration in All-Inorganic Mixed-Halide Perovskite Nanocrystals. *Nat. Commun.* **2019**, *10*, 1–8.
- (11) Brennan, M. C.; Draguta, S.; Kamat, P. V.; Kuno, M. Light-Induced Anion Phase Segregation in Mixed Halide Perovskites. *ACS Energy Lett.* **2018**, *3*, 204–213.
- (12) Xu, B.; Wang, W.; Zhang, X.; Liu, H.; Zhang, Y.; Mei, G.; Chen, S.; Wang, K.; Wang, L.; Sun, X. W. Electric Bias Induced Degradation in Organic-Inorganic Hybrid Perovskite Light-Emitting Diodes. *Sci. Rep.* **2018**, *8*, 1–7.
- (13) Huang, Y.; Yin, W.-J.; He, Y. Intrinsic Point Defects in Inorganic Cesium Lead Iodide Perovskite CsPbI₃. *J. Phys. Chem. C* **2018**, *122*, 1345–1350.
- (14) Kang, J.; Wang, L.-W. High Defect Tolerance in Lead Halide Perovskite CsPbBr₃. *J. Phys. Chem. Lett.* **2017**, *8*, 489–493.
- (15) Walsh, A.; Stranks, S. D. Taking Control of Ion Transport in Halide Perovskite Solar Cells. *ACS Energy Lett.* **2018**, *3*, 1983–1990.
- (16) Eames, C.; Frost, J. M.; Barnes, P. R. F.; O'Regan, B. C.; Walsh, A.; Islam, M. S. Ionic Transport in Hybrid Lead Iodide Perovskite Solar Cells. *Nat. Commun.* **2015**, *6*, 1–8.
- (17) Yang, D.; Ming, W.; Shi, H.; Zhang, L.; Du, M.-H. Fast Diffusion of Native Defects and Impurities in Perovskite Solar Cell Material CH₃NH₃PbI₃. *Chem. Mater.* **2016**, *28*, 4349–4357.
- (18) El-Mellouhi, F.; Rashkeev, S. N.; Marzouk, A.; Kabanal, L.; Belaidi, A.; Merzougui, B.; Tabet, N.; Alharbi, F. H. Intrinsic Stability Enhancement and Ionic Migration Reduction by Fluorinated Cations Incorporated in Hybrid Lead Halide Perovskites. *J. Mater. Chem. C* **2019**, *7*, 5299–5306.
- (19) Yang, R. X.; Skelton, J. M.; da Silva, E. L.; Frost, J. M.; Walsh, A. Spontaneous Octahedral Tilting in the Cubic Inorganic Cesium

Halide Perovskites CsSnX₃ and CsPbX₃ (X = F, Cl, Br, I). *J. Phys. Chem. Lett.* **2017**, *8*, 4720–4726.

(20) Shojaei, F.; Yin, W.-J. Stability Trend of Tilted Perovskites. *J. Phys. Chem. C* **2018**, *122*, 15214–15219.

(21) El-Mellouhi, F.; Marzouk, A.; Bentría, E. T.; Rashkeev, S. N.; Kais, S.; Alharbi, F. H. Hydrogen Bonding and Stability of Hybrid Organic–Inorganic Perovskites. *ChemSusChem* **2016**, *9*, 2648–2655.

(22) Lai, M.; Obliger, A.; Lu, D.; Kley, C. S.; Bischak, C. G.; Kong, Q.; Lei, T.; Dou, L.; Ginsberg, N. S.; Limmer, D. T.; Yang, P. Intrinsic Anion Diffusivity in Lead Halide Perovskites Is Facilitated by a Soft Lattice. *Proc. Natl. Acad. Sci. U. S. A.* **2018**, *115*, 11929–11934.

(23) Oranskaia, A.; Yin, J.; Bakr, O. M.; Brédas, J.-L.; Mohammed, O. F. Halogen Migration in Hybrid Perovskites: The Organic Cation. *J. Phys. Chem. Lett.* **2018**, *9*, 5474–5480.

(24) Marronnier, A.; Roma, G.; Boyer-Richard, S.; Pedesseau, L.; Jancu, J.-M.; Bonnassieux, Y.; Katan, C.; Stoumpos, C. C.; Kanatzidis, M. G.; Even, J. Anharmonicity and Disorder in the Black Phases of Cesium Lead Iodide Used for Stable Inorganic Perovskite Solar Cells. *ACS Nano* **2018**, *12*, 3477–3486.

(25) Liang, J.; et al. All-Inorganic Perovskite Solar Cells. *J. Am. Chem. Soc.* **2016**, *138*, 15829–15832.

(26) Senocrate, A.; Kim, G. Y.; Grätzel, M.; Maier, J. Thermochemical Stability of Hybrid Halide Perovskites. *ACS Energy Lett.* **2019**, *4*, 2859–2870.

(27) McGovern, L.; Futscher, M. H.; Muscarella, L. A.; Ehrler, B. Understanding the Stability of MAPbBr₃ versus MAPbI₃: Suppression of Methylammonium Migration and Reduction of Halide Migration. *J. Phys. Chem. Lett.* **2020**, *11*, 7127–7132.

(28) Pont, S.; Bryant, D.; Lin, C.-T.; Aristidou, N.; Wheeler, S.; Ma, X.; Godin, R.; Haque, S. A.; Durrant, J. R. Tuning CH₃NH₃Pb(1-xBr_x)₃ Perovskite Oxygen Stability in Thin Films and Solar Cells. *J. Mater. Chem. A* **2017**, *5*, 9553–9560.

(29) Kresse, G.; Furthmüller, J. Efficient Iterative Schemes for Ab Initio Total-Energy Calculations Using a Plane-Wave Basis Set. *Phys. Rev. B: Condens. Matter Mater. Phys.* **1996**, *54*, 11169–11186.

(30) Blöchl, P. E. Projector Augmented-Wave Method. *Phys. Rev. B: Condens. Matter Mater. Phys.* **1994**, *50*, 17953–17979.

(31) Perdew, J. P.; Burke, K.; Ernzerhof, M. Generalized Gradient Approximation Made Simple. *Phys. Rev. Lett.* **1996**, *77*, 3865–3868.

(32) Henkelman, G.; Uberuaga, B. P.; Jónsson, H. A Climbing Image Nudged Elastic Band Method for Finding Saddle Points and Minimum Energy Paths. *J. Chem. Phys.* **2000**, *113*, 9901–9904.

(33) Ong, S. P.; Richards, W. D.; Jain, A.; Hautier, G.; Kocher, M.; Cholia, S.; Gunter, D.; Chevrier, V. L.; Persson, K. A.; Ceder, G. Python Materials Genomics (Pymatgen): A Robust, Open-Source Python Library for Materials Analysis. *Comput. Mater. Sci.* **2013**, *68*, 314–319.

(34) Svane, K. L.; Forse, A. C.; Grey, C. P.; Kieslich, G.; Cheetham, A. K.; Walsh, A.; Butler, K. T. How Strong Is the Hydrogen Bond in Hybrid Perovskites? *J. Phys. Chem. Lett.* **2017**, *8*, 6154–6159.

(35) Van der Ven, A.; Ceder, G.; Asta, M.; Tepeš, P. D. First-Principles Theory of Ionic Diffusion with Nondilute Carriers. *Phys. Rev. B: Condens. Matter Mater. Phys.* **2001**, *64*, 184307.

(36) Klarbring, J. Low-Energy Paths for Octahedral Tilting in Inorganic Halide Perovskites. *Phys. Rev. B: Condens. Matter Mater. Phys.* **2019**, *99*, 104105.

(37) Young, J.; Rondinelli, J. M. Octahedral Rotation Preferences in Perovskite Iodides and Bromides. *J. Phys. Chem. Lett.* **2016**, *7*, 918–922.

(38) Whalley, L. D.; Skelton, J. M.; Frost, J. M.; Walsh, A. Phonon Anharmonicity, Lifetimes, and Thermal Transport in $\text{CH}_3\text{NH}_3\text{PbI}_3$ from Many-Body Perturbation Theory. *Phys. Rev. B: Condens. Matter Mater. Phys.* **2016**, *94*, 220301.

(39) Beecher, A. N.; Semonin, O. E.; Skelton, J. M.; Frost, J. M.; Terban, M. W.; Zhai, H.; Alatas, A.; Owen, J. S.; Walsh, A.; Billinge, S. J. L. Direct Observation of Dynamic Symmetry Breaking above Room Temperature in Methylammonium Lead Iodide Perovskite. *ACS Energy Lett.* **2016**, *1*, 880–887.

(40) Luo, Y.; Khoram, P.; Brittman, S.; Zhu, Z.; Lai, B.; Ong, S. P.; Garnett, E. C.; Fenning, D. P. Direct Observation of Halide Migration and Its Effect on the Photoluminescence of Methylammonium Lead Bromide Perovskite Single Crystals. *Adv. Mater.* **2017**, *29*, 1703451.

(41) Zhou, W.; Zhao, Y.; Zhou, X.; Fu, R.; Li, Q.; Zhao, Y.; Liu, K.; Yu, D.; Zhao, Q. Light-Independent Ionic Transport in Inorganic Perovskite and Ultrastable Cs-Based Perovskite Solar Cells. *J. Phys. Chem. Lett.* **2017**, *8*, 4122–4128.

(42) Tennyson, E. M.; Roose, B.; Garrett, J. L.; Gong, C.; Munday, J. N.; Abate, A.; Leite, M. S. Cesium-Incorporated Triple Cation Perovskites Deliver Fully Reversible and Stable Nanoscale Voltage Response. *ACS Nano* **2019**, *13*, 1538–1546.

(43) Yang, M.; Wang, N.; Zhang, S.; Zou, W.; He, Y.; Wei, Y.; Xu, M.; Wang, J.; Huang, W. Reduced Efficiency Roll-Off and Enhanced Stability in Perovskite Light-Emitting Diodes with Multiple Quantum Wells. *J. Phys. Chem. Lett.* **2018**, *9*, 2038–2042.

(44) Capitani, F.; Marini, C.; Caramazza, S.; Dore, P.; Pisanu, A.; Malavasi, L.; Nataf, L.; Baudelet, F.; Brubach, J.-B.; Roy, P.; Postorino, P. Locking of Methylammonium by Pressure-Enhanced H-Bonding in (CH₃NH₃)PbBr₃ Hybrid Perovskite. *J. Phys. Chem. C* **2017**, *121*, 28125–28131.

(45) Francisco-López, A.; Charles, B.; Weber, O. J.; Alonso, M. I.; Garriga, M.; Campoy-Quiles, M.; Weller, M. T.; Goñi, A. R. Pressure-Induced Locking of Methylammonium Cations versus Amorphization in Hybrid Lead Iodide Perovskites. *J. Phys. Chem. C* **2018**, *122*, 22073–22082.

(46) Ghosh, D.; Walsh Atkins, P.; Islam, M. S.; Walker, A. B.; Eames, C. Good Vibrations: Locking of Octahedral Tilting in Mixed-Cation Iodide Perovskites for Solar Cells. *ACS Energy Lett.* **2017**, *2*, 2424–2429.

(47) Gallop, N. P.; Selig, O.; Giubertoni, G.; Bakker, H. J.; Rezus, Y. L. A.; Frost, J. M.; Jansen, T. L. C.; Lovrincic, R.; Bakulin, A. A. Rotational Cation Dynamics in Metal Halide Perovskites: Effect on Phonons and Material Properties. *J. Phys. Chem. Lett.* **2018**, *9*, 5987–5997.

(48) Matsui, T.; Seo, J.-Y.; Saliba, M.; Zakeeruddin, S. M.; Grätzel, M. Room-Temperature Formation of Highly Crystalline Multication Perovskites for Efficient, Low-Cost Solar Cells. *Adv. Mater.* **2017**, *29*, 1606258.